forests

MDPI

Article

Long-Term Vegetation Dynamics and Seasonal Drivers in the Fen River Basin Revealed by kNDVI

Kaijie Niu [1,2], Houfa Wu [3], Weisheng Zhang [1,2] and Cun Zhan [4,*]

[1] School of Geographical Sciences, Taiyuan Normal University, Jinzhong 030619, China; niukaijie@tynu.edu.cn (K.N.); hsqs24@126.com (W.Z.)
[2] Shanxi Key Laboratory for Surface Processes and Resource Ecological Security in Fen River Basin, Jinzhong 030619, China
[3] Changjiang Institute of Survey, Planning, Design and Research, Wuhan 430010, China; wuhoufa@cjwsjy.com.cn
[4] Faculty of Electric Power Engineering, Kunming University of Science and Technology, Kunming 650500, China
* Correspondence: zhancun@kust.edu.cn

Abstract

Large-scale ecological restoration has substantially altered vegetation patterns in many environmentally sensitive regions, yet how the relative importance of climatic and non-climatic influences varies among seasons remains insufficiently understood. This study investigated long-term vegetation dynamics and their seasonal drivers in the Fen River Basin, China, using kernel Normalized Difference Vegetation Index (kNDVI) derived from the GIMMS-3G+ dataset for 1982–2022. Trend analysis, partial and multiple correlation analyses, residual trend analysis, and land-use change information were integrated to characterize vegetation changes and assess the relative contributions of climatic and residual-based anthropogenic influences. The results showed widespread vegetation greening across the basin. Growing-season kNDVI increased significantly at a rate of 0.0029 yr^{-1}, with significant increases occurring over 90.74% of the basin, while the mean growing-season kNDVI after 2000 was 23.1% higher than that before 2000. Precipitation showed the strongest overall relationship with vegetation, with positive correlations across 92.86% of the basin, whereas solar radiation exhibited relatively weak associations. Residual-based attribution further revealed pronounced seasonal differences in vegetation drivers. The climate-predicted component accounted for 55.9% of the attributed vegetation greening in spring, whereas the residual component accounted for larger relative shares in summer (60.3%) and autumn (61.7%). Over the entire growing season, the climate-predicted and residual components accounted for 41.6% and 58.4% of the attributed greening, respectively. Land-use transitions after 2000, particularly farmland-to-forest and farmland-to-grassland conversions, provided additional evidence consistent with a possible contribution of ecological restoration to vegetation recovery. Overall, the results reveal a clear seasonal shift from stronger climatic control in spring toward increasing residual-based anthropogenic influences in summer and autumn. This study demonstrates the value of integrating long-term kNDVI remote sensing, seasonal attribution, and land-use information for monitoring vegetation recovery and supporting adaptive ecosystem management in ecologically sensitive regions.

Keywords: kernel NDVI; vegetation dynamics; Grain for Green Program; seasonal attribution; land-use change; Fen River Basin

Check for updates

Academic Editor: Uroš Durlević

Received: 17 September 2026
Revised: 11 October 2026
Accepted: 13 October 2026
Published: 16 October 2026

Copyright: © 2026 by the authors. Licensee MDPI, Basel, Switzerland. This article is an open access article distributed under the terms and conditions of the Creative Commons Attribution (CC BY) license.

1. Introduction

Vegetation dynamics critically govern terrestrial ecosystem functioning by mediating atmosphere–soil–water exchanges, regulating biogeochemical cycles, and sustaining biodiversity and human livelihoods [1,2]. Spatiotemporal vegetation patterns are fundamentally shaped by climate drivers and exhibit high sensitivity to synergistic climate change and anthropogenic forcing [3–5]. Satellite observations confirm widespread greening trends across regional to global scales, underscoring the necessity to quantify the drivers of these changes—particularly regarding the spatiotemporal heterogeneity of driving factors and the relative contributions of climatic versus anthropogenic influences [6,7]. Precise attribution is vital for formulating evidence-based land management and ecological conservation strategies, as well as supporting agricultural land-suitability assessment and regional land-use planning [8,9].

Spatiotemporal heterogeneity complicates large-scale vegetation monitoring via traditional methods. Remote sensing overcomes this by providing continuous, high-resolution data essential for tracking vegetation dynamics [10,11], primarily through indices like the Normalized Difference Vegetation Index (NDVI), Leaf Area Index (LAI), and Enhanced Vegetation Index (EVI) [12,13]. While NDVI correlates strongly with vegetation biophysical parameters (e.g., green biomass), it suffers from saturation and canopy background interference in dense vegetation [14]. EVI mitigates soil/aerosol noise but retains saturation limitations [15]. In contrast, the kernel-based NDVI (kNDVI) demonstrates superior performance: it achieves higher sensitivity to vegetation changes, enhanced robustness to noise and seasonal variability, and eliminates saturation effects plaguing NDVI and EVI [16,17]. Consequently, kNDVI has emerged as a validated standard for long-term trend analysis in critical regions like the Yellow River Basin, Yangtze River Basin, and Loess Plateau [18–20].

The biogeochemical coupling between climate change and terrestrial ecosystems dominates contemporary environmental research [21–23]. Precipitation, temperature, and solar radiation constitute the primary climatic regulators of vegetation dynamics [24–26]. Global warming has triggered pronounced greening trends, particularly across Northern Hemisphere ecosystems, where rising temperatures extend the alpine growing season [27–32]. Conversely, arid-region vegetation exhibits heightened vulnerability to precipitation variability due to water stress [33,34], while solar radiation fundamentally constrains photosynthetic efficiency [35]. Anthropogenic forcing further modulates these patterns: initiatives like afforestation and returning farmland to forests enhance vegetation cover [10,36], whereas urbanization, cropland expansion, and deforestation drive significant degradation [37,38]. This dualistic influence—where climate and human drivers alternately amplify or suppress vegetation productivity—necessitates quantitative attribution to guide targeted conservation strategies.

In response to widespread ecosystem deterioration across northern China, authorities implemented the Grain for Green Program (GGP) in 1999, while pilot work started in partial counties of the Shanxi Province in 2000 [39]. This nationwide conservation strategy systematically converts marginal farmlands to forest and grassland ecosystems. Numerous studies have documented the program's substantial ecological benefits in this region [40–42]; nevertheless, there remain certain research gaps regarding vegetation dynamics and their driving mechanisms in northern China. Most studies rely exclusively on either GIMMS NDVI3g (1982–2015) [43,44] or MODIS NDVI (2000–present) [45,46] datasets while frequently neglecting the critical issue of NDVI saturation. Meanwhile, although temperature and precipitation have been widely recognized as dominant climatic drivers, the influence of solar radiation on vegetation dynamics remains understudied [47]. To address the above-mentioned limitations, our previous study constructed a 41-year continuous NDVI time series from a unified data source and adopted the kNDVI index

to mitigate the critical NDVI saturation issue [48]. Furthermore, solar radiation was incorporated as one of the major climatic drivers. Building on this work, interannual and growing-season vegetation variations as well as their climatic response characteristics across the Fen River Basin were investigated. Nevertheless, systematic investigations into seasonal-scale vegetation dynamics and their climatic drivers remain limited. In particular, divergent vegetation responses to climatic factors across distinct phenological stages have not been fully elucidated. These knowledge gaps impede our ability to fully understand vegetation–climate interactions at finer temporal scales.

The FRB, an ecologically vulnerable semi-arid sub-basin within the Yellow River system, serves as a representative case of these challenges. Despite documented GGP successes, drivers of long-term vegetation dynamics in the FRB remain unquantified due to insufficient monitoring and methodological constraints. Although residual trend analysis (RESTREND) has been widely applied to separate climatic and anthropogenic contributions to vegetation dynamics, the interpretation of residual components requires caution. The residual represents vegetation variation unexplained by the selected climatic variables and may include anthropogenic signals as well as other factors not explicitly considered in the model, including land-use change, ecological disturbances, soil conditions, nonlinear vegetation–climate relationships, satellite-observation uncertainty, and model uncertainty. Nevertheless, in regions experiencing strong ecological restoration programs and human-induced land management changes, residual trends are commonly used as an effective proxy for estimating anthropogenic influences when comprehensive long-term human activity datasets are unavailable. Therefore, residual-based attribution should be understood as a relative contribution assessment within the RESTREND framework rather than an absolute quantification of human impacts. To resolve this, we introduce an integrated approach: deriving kernel NDVI (kNDVI) from more than 40 years of continuous NDVI data (1982–2022), enabling robust pre-GGP (1982–1999) and post-GGP (2000–2022) comparisons; incorporating solar radiation alongside precipitation/temperature in climate-vegetation responses; and implementing seasonal-scale attribution analysis. Our objectives are to:

(1) Characterize multiscale spatiotemporal heterogeneity in kNDVI and climatic drivers;
(2) Diagnose dynamic climate–vegetation responses and identify dominant controls;
(3) Quantitatively partition the relative contributions of climatic factors and residual-based anthropogenic influences to observed vegetation dynamics in the FRB.

This work advances the attribution framework through the application of kNDVI and the incorporation of solar radiation as an additional climatic driver, providing policy-relevant information for adaptive ecosystem management in climate-sensitive basins.

2. Materials and Methods

2.1. Study Area

The Fen River Basin (FRB; 35.22–39.07° N, 110.45–113.45° E) encompasses 39,741 km^2 across the central and southwestern Shanxi Province, forming a critical part of the eastern Yellow River Basin (YRB). As the second-largest tributary of the Yellow River (716 km length), it exhibits pronounced topographic heterogeneity: elevation decreases north-to-south across mountain, hill, basin, and plain terrains. Key socioeconomic zones include the highly urbanized Taiyuan Basin (provincial capital) and the agriculturally intensive Linfen Basin—Shanxi's primary irrigation district. Climatically, the FRB experiences a temperate continental monsoon regime (mean annual temperature: 11 °C; precipitation: 400–600 mm). Dominant land cover comprises cropland (mid-low elevations), forests, and grasslands (upper basins/plateau highlands) (Figure 1). Functionally, the FRB sustains 41% of Shanxi's population and drives provincial economic activity while serving as a critical ecological

buffer for the Yellow River Basin. Its location within an arid/semi-arid ecotone, coupled with intensive land-use pressures, renders it exceptionally vulnerable to climate–human perturbations—establishing the FRB as a strategic model system for studying coupled ecohydrological dynamics.

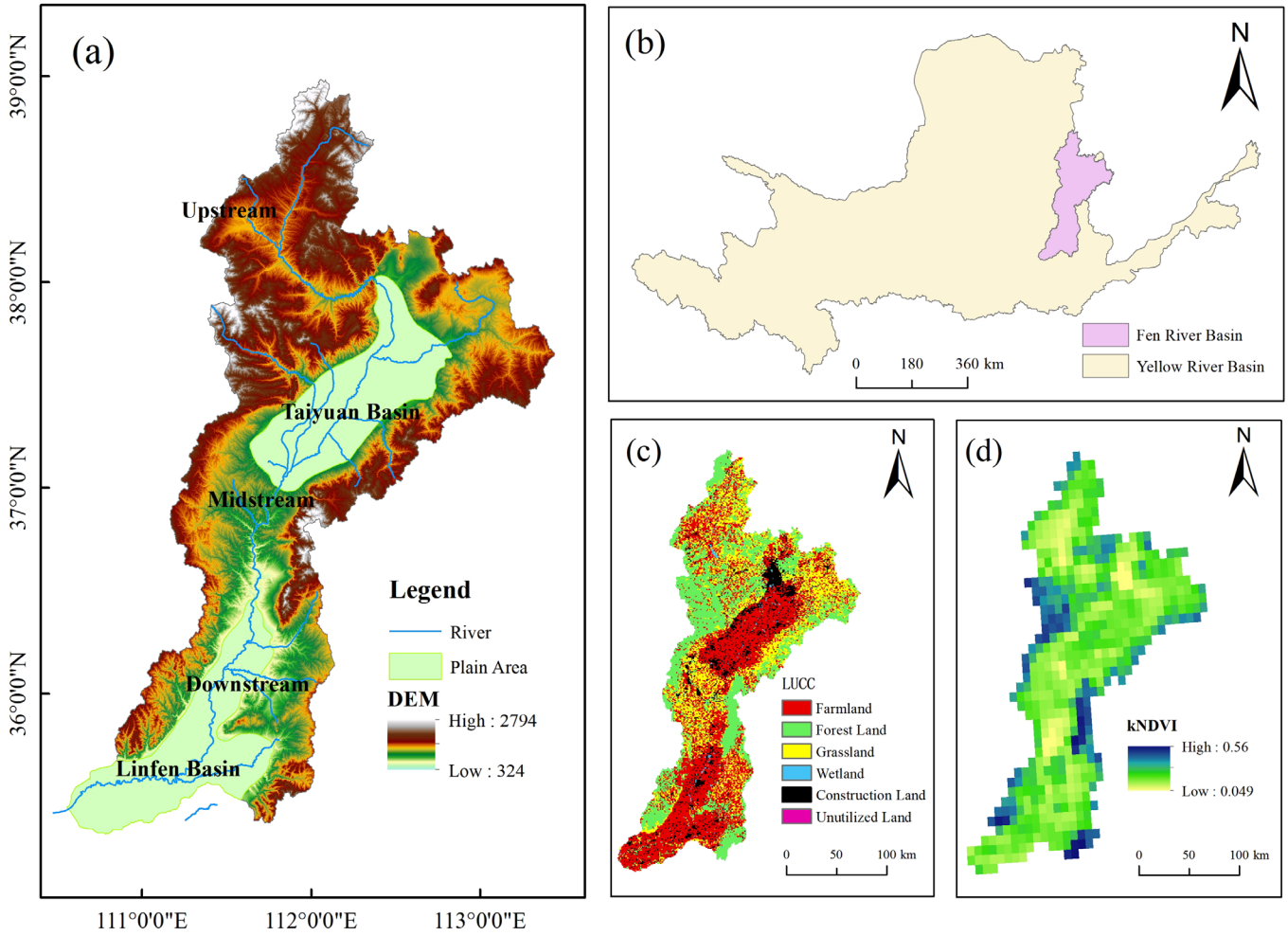


Figure 1. Spatial maps illustrate (**a**) the topographical categorization, (**b**) the spatial arrangement at Yellow River Basin, (**c**) the LUCC distribution, and (**d**) the kNDVI distribution in the Fen River Basin.

The Fen River Basin was selected as the study area because it exhibits substantial topographic and hydroclimatic heterogeneity, together with contrasting land-use patterns and human disturbances. The basin encompasses mountainous areas, agricultural landscapes, highly urbanized regions, and areas affected by ecological restoration. These characteristics make it a suitable region for examining the spatial and seasonal variability of vegetation dynamics and their relationships with climatic and non-climatic factors.

2.2. Data

2.2.1. NDVI Data

The GIMMS-3G+ NDVI dataset, obtained from the Distributed Active Archive Center (DAAC) at Oak Ridge National Laboratory, integrates Advanced Very High- Resolution Radiometer (AVHRR) observations from multiple satellites. This global-coverage dataset (0.0833° spatial resolution; biweekly temporal resolution from 1982 to 2022) incorporates corrections for sensor calibration degradation, orbital drift, and volcanic aerosol effects. We processed the data by (1) deriving monthly maximum value composites to minimize atmospheric contamination, (2) applying Savitzky–Golay filtering to reduce noise [49],

and (3) calculating seasonal NDVI averages (spring: March–May; summer: June–August; autumn: September–November), with April–October representing the full growing season.

2.2.2. Climate Data

Climate data acquisition and processing involved:

- Precipitation (PRE) and temperature (TEM): Obtained from Peng et al. with 1 km resolution monthly datasets for China (1901–2022), generated through Delta downscaling of CRU and WorldClim data with 496-station validation [50]. The data were originally released for 1901–2017 and later temporally extended to 2022 by the data provider [51,52].
- Solar radiation (SR): Acquired from TerraClimate (1958–2022) with 4 km resolution [53]. The data was available at the website [54].

To ensure spatial consistency between climatic predictors and vegetation observations, all climatic variables were resampled to the GIMMS-3G+ grid (0.0833°) using bilinear interpolation. This harmonization was required for pixel-wise vegetation–climate correlation and attribution analyses and provides climatic estimates at the spatial scale of the kNDVI observations. However, the resampled data do not fully represent sub-grid climatic variability, particularly in areas with complex topography.

2.2.3. Land Use Data

The land use data were acquired from the Resource and Environmental Science Data Platform (https://www.resdc.cn/). The land-use dataset was available at five-year intervals beginning in 1980. Because land-use maps were not available for the exact initial and final years of the vegetation record (1982 and 2022), and the 1980 and 2020 maps were used as the nearest available temporal proxies. Land-use transitions were analyzed for 1980–2000, 2000–2020, and 1980–2020.

2.2.4. Topographical Data

Topographic information was obtained from the 30 m Shuttle Radar Topography Mission (SRTM) digital elevation model (DEM). The DEM was used solely to characterize and visualize the topographic setting of the Fen River Basin and to prepare the study area map. It was not resampled to the GIMMS-3G+ grid or included as a predictor in the vegetation–climate correlation and attribution analyses.

2.3. Methods

2.3.1. kNDVI Calculation

The kernel NDVI (kNDVI) was computed using a nonlinear kernel approach:

$$kNDVI = \frac{k(n,n) - k(n,r)}{k(n,n) + k(n,r)} \quad (1)$$

The parameter k can be expressed as:

$$k(n,r) = \exp\left(-\left(n-r\right)^2 / \left(\left(2\sigma^2\right)\right)\right) \quad (2)$$

where NIR (n) represents the reflectance of the NIR; red (r) represents the red bands, respectively; σ calculates the separation between n and r; Equation (1) can be expressed as:

$$kNDVI = \frac{1 - k(n,r)}{1 + k(n,r)} = \tanh\left(\left(\frac{n-r}{2\sigma}\right)^2\right) \quad (3)$$

Considering the NIR and red bands are at an equal distance, Equation (3) can be simplified to:

$$kNDVI = \tanh\left(NDVI^2\right) \tag{4}$$

In our study, Equation (4) can be employed to calculate the monthly kNDVI values. The values can be derived by averaging the growing season and spring, summer, and autumn.

2.3.2. Trend Test

The Theil–Sen estimator [55], a robust nonparametric approach for trend estimation, was employed in this analysis. The mathematical formulation is expressed as:

$$\beta = \text{median}\left(\frac{kNDVI_j - kNDVI_i}{j - i}\right), \forall\, i < j \tag{5}$$

The nonparametric Mann–Kendall (MK) test was employed to assess temporal trends in vegetation (kNDVI) and climatic variables across the Fen River Basin at pixel-level resolution. The MK test was applied to all pixels containing complete kNDVI time series of length n.

$$Z_s = \begin{cases} \frac{S-1}{\sqrt{\text{Var}(S)}}, & S > 0 \\ 0, & S = 0 \\ \frac{S+1}{\sqrt{\text{Var}(S)}}, & S < 0 \end{cases} \tag{6}$$

$$S = \sum_{i=1}^{n-1} \sum_{j=i+1}^{n} \text{sgn}\left(kNDVI_j - kNDVI_i\right) \tag{7}$$

$$\text{Var}(s) = \frac{n(n-1)(2n+5) - \sum_{i=1}^{p} t_j\left(t_j - 1\right)\left(2t_j + 5\right)}{18} \tag{8}$$

$$\text{sgn}\left(x_j - x_i\right) = \begin{cases} 1 & x_j - x_i > 0 \\ 0 & x_j - x_i = 0 \\ -1 & x_j - x_i < 0 \end{cases} \tag{9}$$

Here, $kNDVI_i$ and $kNDVI_j$ denote the vegetation indices for years i and j, respectively. The sgn is a symbolic function and serves as the sign operator. The parameter p indicates the total number of tied groups in the dataset, while i-th represents the count of data points within the j-th tied group. Trend significance was evaluated at 90% confidence ($|Z| > 1.64$), 95% confidence ($|Z| > 1.96$), and 99% confidence ($|Z| > 2.58$). The Theil–Sen estimator was used to quantify the magnitude and direction of the temporal trends, whereas the Mann–Kendall test was used to assess their statistical significance. Three significance thresholds ($p < 0.10$, $p < 0.05$, and $p < 0.01$) were adopted to indicate progressively stronger statistical evidence against the null hypothesis, rather than the magnitude or strength of vegetation trends.

To account for temporal autocorrelation, the Mann–Kendall (MK) test was modified using the effective sample size (ESS) approach [56]. For each variable and season, the 1982–2022 time series was first detrended using the Sen slope, and the lag-one autocorrelation was estimated from the detrended series. Under an AR(1) approximation, the estimated autocorrelation was used to calculate the effective sample size and adjust the variance of the MK statistic, thereby providing autocorrelation-adjusted significance levels. The original Sen slopes and MK statistics were retained, ensuring that the correction affected statistical significance rather than the estimated trend magnitude or direction. The resulting ESS-adjusted p-values were used to update the significance classifications in Mann-Kendall trend test. This correction addresses temporal autocorrelation but does

not account for spatial multiple testing; therefore, the reported significance levels remain pixel-wise estimates.

2.3.3. Partial Correlation Analysis

The observed bivariate correlations between vegetation dynamics (kNDVI) and climatic variables may be confounded by covarying environmental influences. To mitigate this, we employed partial correlation analysis (PCC), which statistically controls for two additional confounding factors, thereby providing more accurate estimates of climate–vegetation relationships. The PCC calculation procedure comprised three key steps [5]:

$$R_{xy} = \frac{\sum_{i=1}^{n}[(x_i - \overline{x})(y_i - \overline{y})]}{\sqrt{\sum_{i=1}^{n}(x_i - \overline{x})^2}\sqrt{\sum_{i=1}^{n}(y_i - \overline{y})^2}} \tag{10}$$

$$R_{xy,z} = \frac{R_{xy} - R_{xz} \times R_{yz}}{\sqrt{(1 - R_{xz}^2)\left(1 - R_{yz}^2\right)}} \tag{11}$$

$$R_{xy,zw} = \frac{R_{xy,z} - R_{xw,z}R_{yw,z}}{\sqrt{\left(1 - R_{xw,z}^2\right)\left(1 - R_{yw,z}^2\right)}} \tag{12}$$

Here, R_{xy} represents the correlation coefficient between x and y; $R_{xy,z}$ denotes the partial correlation between x and y while controlling for z; $R_{xy,zw}$ denotes the partial correlation between x and y controlling for both w and z. The statistical significance of all partial correlations was assessed using two-tailed Student's t-tests.

$$t = R\sqrt{\frac{n - k - 2}{1 - R^2}} \tag{13}$$

Here, n represents the number of observations, k signifies the number of controlled variables (k = 2 in this study). The degrees of freedom are $n - k - 2$, where n is the number of observations and k is the number of controlled variables. For the pixel-wise analysis, significance was corrected for multiple comparisons using the Benjamini–Hochberg FDR [57]. Statistical significance was defined as $q < 0.05$, where q denotes the BH-adjusted p-value.

2.3.4. Multiple Correlation Analysis

Multivariate correlation analysis was employed to assess the combined influence of three climatic drivers (temperature, precipitation, and solar radiation) on vegetation dynamics (kNDVI). This approach quantifies the joint explanatory power of multiple predictors through the multivariate correlation coefficients (MCCs), while controlling for inter-variable dependencies [58].

$$R_{x,yzw} = \sqrt{1 - \left(1 - R_{xy}^2\right)\left(1 - R_{xz,y}^2\right)\left(1 - R_{xw,yz}^2\right)} \tag{14}$$

$$F = \frac{R_{x,yzw}^2}{1 - R_{x,yzw}^2} \times \frac{n - k - 1}{k} \tag{15}$$

Here, the multiple correlation coefficient ($R_{x,yzw}$) measures the collective linear association between response variable x and predictor set $\{y, z, w\}$. Its statistical significance was evaluated using F-tests, with n indicating sample size and k denoting the quantity of explanatory variables.

2.3.5. Residual Trend Analysis

Residual trend analysis (RESTREND) is widely used to investigate vegetation dynamics by distinguishing the component statistically explained by selected climatic variables from the unexplained residual component. In this study, the analysis involved two steps: (1) establishing a multiple linear regression model between observed kNDVI and climatic variables (precipitation, temperature, and solar radiation) to estimate climate-predicted kNDVI; (2) calculating the residuals as the differences between observed and predicted kNDVI and examining their temporal trends. These residual trends were interpreted as indicators of potential anthropogenic influence rather than direct measures of human activities, as they may also reflect omitted environmental factors, nonlinear climatic responses, observational uncertainty, and model errors.

The model formulation is expressed as:

$$kNDVI = a \times PRE + b \times TEM + c \times SR + \varepsilon \quad (16)$$

$$kNDVI_{res} = kNDVI_{obs} - kNDVI_{pre} \quad (17)$$

Here, $kNDVI_{\text{obs}}$ represents the observed vegetation index values, $kNDVI_{pre}$ indicates the model-predicted kNDVI values, and $kNDVI_{res}$ denotes the residual values (observed–predicted). The regression model incorporates coefficients a, b, and c for PRE, TEM, and SR, respectively; ε is the model intercept/constant term.

Within the RESTREND framework, precipitation (PRE), temperature (TEM), and solar radiation (SR) were assumed to represent the principal climatic predictors of vegetation dynamics. The component predicted by these variables was defined as the climate-related component (CC), whereas the unexplained residual component was used as a proxy for potential anthropogenic influence (RBAI). However, RBAI should not be interpreted as a direct or exclusive measure of human activity, as it may also reflect omitted environmental factors, nonlinear vegetation–climate responses, observational uncertainty, and model errors. Accordingly, the relative contributions of CC and RBAI to observed vegetation changes were estimated using the classification scheme presented in Table 1. These estimates represent a model-dependent statistical decomposition rather than precise causal contributions of climatic and anthropogenic influences.

Table 1. Identification and calculation of the relative contributions of drivers to vegetation variation in the Fen River Basin.

Vegetation Variation	$Slope_{\text{obs}}$	$Slope_{\text{pre}}$	$Slope_{res}$	Relative Contribution of Climate Change (%)	Relative Contribution of Residual-Based Anthropogenic Influences (%)
Greening	>0	<0	<0	0	100
	>0	>0	<0	100	0
	>0	>0	>0	$\frac{Slope_{pre}}{Slope_{\text{obs}}} \times 100\%$	$\frac{Slope_{res}}{Slope_{\text{obs}}} \times 100\%$
Degradation	<0	<0	>0	0	100
	<0	>0	<0	100	0
	<0	<0	<0	$\frac{Slope_{pre}}{Slope_{\text{obs}}} \times 100\%$	$\frac{Slope_{res}}{Slope_{\text{obs}}} \times 100\%$

Note: Relative-contribution percentages are computed pixel-wise using pixel-level slope values of observed kNDVI ($Slope_{\text{obs}}$), climate-predicted kNDVI ($Slope_{pre}$), and residual kNDVI ($Slope_{res}$). $Slope_{\text{obs}}$ = total vegetation trend; $Slope_{pre}$ = trend induced by climate change; $Slope_{res}$ = trend induced by residual-based anthropogenic influences.

3. Results

3.1. Quantitative Analysis and Temporal Dynamics of the Vegetation Index (kNDVI) and Climatic Variables

Table 2 summarizes the statistical characteristics of kNDVI and key climatic parameters (precipitation, mean temperature, and solar radiation) across multiple temporal scales in the FRB. For the growing seasons during the 1982–2022 period, the mean values (±SD) of kNDVI, precipitation, temperature, and solar radiation were 0.254 ± 0.04, 122.26 ± 6.15 mm, 16.78 ± 0.54 °C, and 220.4 ± 7.19 Wm^{-2}, respectively. Among them, the corresponding annual average values from 1982 to 1999 were 0.225 ± 0.015, 118.97 ± 6.65 mm, 16.38 ± 0.42 °C, and 219.55 ± 8.7 Wm^{-2}, while the corresponding annual average values from 2000 to 2022 were 0.277 ± 0.038, 124.83 ± 4.21 mm, 17.09 ± 0.38 °C, and 221.07 ± 5.64 Wm^{-2}. The growing-season kNDVI increased by 23.1% after 2000 compared to the pre-2000 period.

Table 2. Descriptive statistics (mean ± SD) of kNDVI and climatic variables for the growing season and individual seasons during the 1982–1999, 2000–2022, and 1982–2022 periods.

Season	Period	kNDVI Mean ± SD	PRE Mean ± SD	TEM Mean ± SD	SR Mean ± SD
Growing Season	1982~2022	0.254 ± 0.04	122.26 ± 6.15	16.78 ± 0.54	220.4 ± 7.19
	1982~1999	0.225 ± 0.015	118.97 ± 6.65	16.38 ± 0.42	219.55 ± 8.7
	2000~2022	0.277 ± 0.038	124.83 ± 4.21	17.09 ± 0.38	221.07 ± 5.64
Spring	1982~2022	0.143 ± 0.023	108.07 ± 11.34	10.62 ± 0.9	216.47 ± 10.59
	1982~1999	0.127 ± 0.013	99 ± 8.45	9.89 ± 0.65	211.25 ± 9.86
	2000~2022	0.155 ± 0.022	115.16 ± 7.66	11.19 ± 0.63	220.55 ± 9.27
Summer	1982~2022	0.315 ± 0.046	141.8 ± 8.45	21.34 ± 0.66	245.83 ± 11.89
	1982~1999	0.285 ± 0.025	138.16 ± 9.33	20.92 ± 0.57	244.99 ± 13.91
	2000~2022	0.338 ± 0.046	144.65 ± 6.39	21.67 ± 0.52	246.49 ± 10.1
Autumn	1982~2022	0.185 ± 0.033	68.35 ± 5.37	9.37 ± 0.72	152.85 ± 8.35
	1982~1999	0.159 ± 0.014	67.67 ± 5.99	9.08 ± 0.76	154.18 ± 8.25
	2000~2022	0.205 ± 0.029	68.88 ± 4.76	9.6 ± 0.59	151.8 ± 8.28

For the analysis of each season, the annual average values of the kNDVI, precipitation, average temperature, and solar radiation during the spring period from 1982 to 2022 were 0.143 ± 0.023, 108.07 ± 11.34 mm, 10.62 ± 0.9 °C, and 216.47 ± 10.59 Wm^{-2}, respectively. During the summer period, they were 0.315 ± 0.046, 141.8 ± 8.45 mm, 21.34 ± 0.66 °C, and 245.83 ± 11.89 Wm^{-2}, while during the autumn period, they were 0.185 ± 0.033, 68.35 ± 5.37 mm, 9.37 ± 0.72 °C, and 152.85 ± 8.35 Wm^{-2}. When comparing the pre- and post-2000 periods, it was found that except for a slight decrease in solar radiation in autumn, all other factors increased over time in spring, summer, and autumn.

Figure 2 depicts the trends in growing season and seasonal kNDVI, precipitation, temperature, and solar radiation within the FRB from 1982 to 2022. Significant increasing trends were observed for kNDVI (0.0029 yr^{-1}, $p < 0.01$), precipitation (0.25 mm yr^{-1}, $p < 0.05$), and temperature (0.033 °C yr^{-1}, $p < 0.01$), while solar radiation exhibited a non-significant increase (0.138 W m^{-2} yr^{-1}, $p > 0.1$). Seasonally, kNDVI increased significantly in spring (0.0016 yr^{-1}), summer (0.0029 yr^{-1}), and autumn (0.0029 yr^{-1}; all $p < 0.01$), and precipitation increased most markedly in spring (0.615 mm yr^{-1}, $p < 0.01$), exceeding summer (0.274 mm yr^{-1}) and autumn (0.282 mm yr^{-1}; both $p < 0.05$). Temperature rises were higher in spring and summer (both 0.037 °C yr^{-1}, $p < 0.01$) than in autumn (0.027 °C yr^{-1}, $p < 0.01$). However, solar radiation in autumn showed the largest non-significant increase (0.463 W m^{-2} yr^{-1}, $p > 0.1$). A pronounced shift occurred around 2000: pre-2000 kNDVI trends were

near-zero (summer declined), whereas the post-2000 kNDVI increased significantly during the growing season (0.0052 yr^{-1}), spring (0.0028 yr^{-1}), summer (0.0062 yr^{-1}), and autumn (0.0037 yr^{-1}; all $p < 0.01$). Conversely, growing season precipitation, temperature, and solar radiation growth rates pre-2000 (0.483 mm yr^{-1}, 0.045 °C yr^{-1}, and 0.368 W m^{-2} yr^{-1}) were 10.7-fold, 2.25-fold, and 1.55-fold higher, respectively, compared to post-2000 rates, indicating a marked deceleration in meteorological variable increases. Additionally, similar deceleration patterns were evident across individual seasons post-2000.

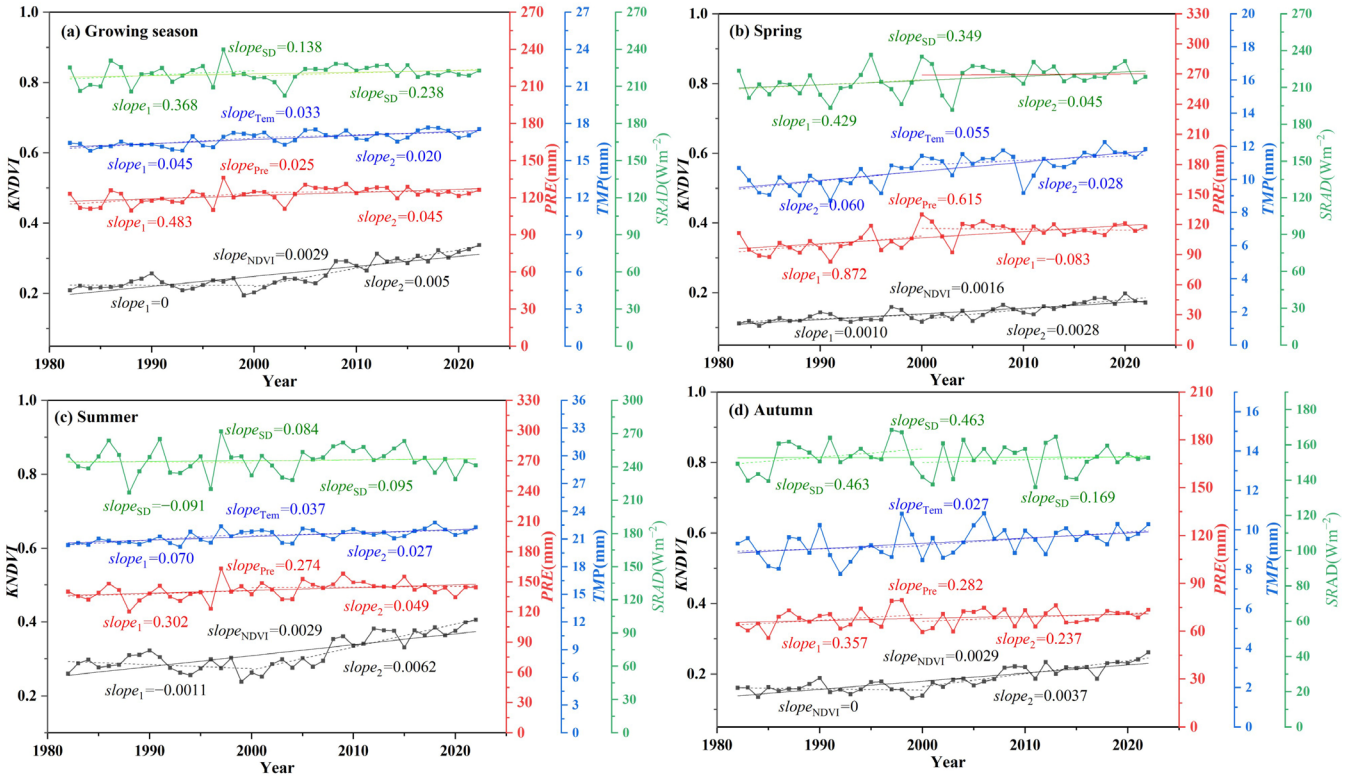


Figure 2. Interannual kNDVI and climatic parameter trends in Fen River Basin (**a**) in growing season, (**b**) in spring, (**c**) in summer, and (**d**) in autumn during the 1982–1999 and 2000–2022 periods and the entire study period (1982–2022).

3.2. Spatiotemporal Patterns of Vegetation Dynamics (kNDVI) and Climatic Variables in the FRB

Over the past four decades, the FRB exhibited pronounced spatial heterogeneity in the trends and persistence (Hurst index, H) of kNDVI, precipitation, mean temperature, and solar radiation (Table 3, Figure 3). During the growing season, 97.55% of the basin area displayed increasing kNDVI trends, with 90.74% showing statistically significant increases ($p < 0.01$). Conversely, only 2.45% of the area exhibited browning trends, which was primarily concentrated in the rapidly urbanizing Jinzhong region (the location of Taiyuan, the provincial capital of Shanxi). Seasonally, the proportion of areas with significant kNDVI increases ($p < 0.01$) varied in the spring (76.98%), summer (81.91%), and autumn (87.36%). Correspondingly, areas exhibiting significant browning ($p < 0.01$) comprised 3.13% (spring), 0.52% (summer), and 0.88% (autumn). Thus, the area with significant increasing kNDVI trends was greatest in autumn, followed by summer and spring. This ordering describes the spatial extent of statistical significance rather than the magnitude of vegetation change.

Table 3. Area percentages of trend and Hurst-index categories for kNDVI, precipitation, temperature, and solar radiation during the growing season and individual seasons.

Variables	Classification	Growing Season				Spring				Summer				Autumn			
		kNDVI	PRE	TEM	SR	kNDVI	PRE	TEM	SR	kNDVI	PRE	TEM	SR	kNDVI	PRE	TEM	SR
MK	$p < 0.01$ (−)	0.88	0.00	0.00	0.00	3.13	0.00	0.00	0.00	0.52	0.00	0.00	0.00	0.88	0.00	0.00	0.00
	$0.01 \leq p < 0.05$ (−)	0.00	0.00	0.00	0.00	2.62	0.00	0.00	0.00	0.53	0.00	0.00	0.00	0.35	0.00	0.00	0.00
	$0.05 \leq p < 0.10$ (−)	0.00	0.00	0.00	0.00	0.88	0.00	0.00	0.00	0.48	0.00	0.00	0.00	0.17	0.00	0.00	0.00
	$p \geq 0.10$ (−)	1.57	0.00	0.00	0.00	4.03	0.00	0.00	0.00	3.69	0.00	0.00	47.67	1.57	0.00	0.00	34.46
	$p \geq 0.10$ (+)	2.79	0.00	0.00	60.13	7.86	0.00	0.00	0.00	4.51	2.37	0.00	32.33	4.53	40.12	0.00	65.54
	$0.05 \leq p < 0.10$ (+)	2.32	0.00	0.00	7.96	1.81	0.00	0.00	0.00	3.01	4.21	0.00	16.51	2.28	16.84	0.00	0.00
	$0.01 \leq p < 0.05$ (+)	1.70	7.60	0.00	4.99	2.69	11.05	0.00	22.35	5.35	16.60	0.00	3.49	2.86	10.04	14.10	0.00
	$p < 0.01$ (+)	90.74	92.40	100.00	26.92	76.98	88.95	100.00	77.65	81.91	76.82	100.00	0.00	87.36	33.00	85.90	0.00
HURST	$H \leq 0.5$	0.88	0.00	0.00	23.12	0.88	0.00	0.00	0.00	0.35	0.00	0.00	6.30	6.30	38.88	0.00	0.35
	$H > 0.5$	99.12	100.00	100.00	76.88	99.12	100.00	100.00	100.00	99.65	100.00	100.00	93.70	93.70	61.12	100.00	99.65

Note: Positive (+) and negative (−) signs denote increasing and decreasing trends, respectively; *p*-values indicate statistical significance derived from Mann–Kendall tests.

Growing-season temperature increased significantly throughout the raster mask ($p < 0.01$), whereas precipitation increased at $p < 0.01$ over 92.40% of the area and at $p < 0.05$ over 100.00%. Solar radiation increased significantly ($p < 0.05$) in 31.91% of the basin, including 26.92%, significant at $p < 0.01$, predominantly in the southern regions. Seasonal climate trends also differed. In spring, temperature increased at $p < 0.01$ throughout the raster mask, while precipitation increased at $p < 0.01$ over 88.95% and at $p < 0.05$ over 100.00% of the area. Solar radiation increased at $p < 0.01$ over 77.65% and at $p < 0.05$ over 100.00% of the area. In summer, significant precipitation increases covered 93.42% of the area ($p < 0.05$), while temperature increased at $p < 0.01$ throughout the raster mask. Significant solar-radiation increases occupied 3.49% of the area ($p < 0.05$); 47.67% exhibited nonsignificant decreases and 32.33% exhibited nonsignificant increases ($p \geq 0.10$), while a further 16.51% showed marginally significant increases ($0.05 \leq p < 0.10$). In autumn, significant precipitation increases covered 43.04% of the area ($p < 0.05$). Temperature increased at $p < 0.01$ over 85.90% and at $p < 0.05$ over 100.00% of the area. Solar-radiation trends were nonsignificant throughout the raster mask, with 65.54% showing increases and 34.46% showing decreases ($p \geq 0.10$).

Hurst analysis revealed widespread persistence in kNDVI across the Fen River Basin (Figure 4). During the growing season, $H > 0.5$ for kNDVI occurred across >99% of the basin, indicating enhanced long-term persistence. An H value greater than 0.5 indicates persistence in the temporal behavior of the kNDVI series. When interpreted jointly with the Theil–Sen slope, $H > 0.5$ combined with a positive slope indicates persistence of the observed greening tendency, whereas $H > 0.5$ combined with a negative slope indicates persistence of the observed browning tendency. The proportion of the basin with $H > 0.5$ was 99.12% for the growing season. Among the individual seasons, the corresponding proportions were 99.65% in summer, 99.12% in spring, and 93.70% in autumn (Table 3). Temperature exhibited universal persistence ($H > 0.5$) across 100% of the basin during the growing season and all individual seasons, and precipitation persistence ($H > 0.5$) was observed in 100% of the basin for all the study periods except autumn (61.1%).

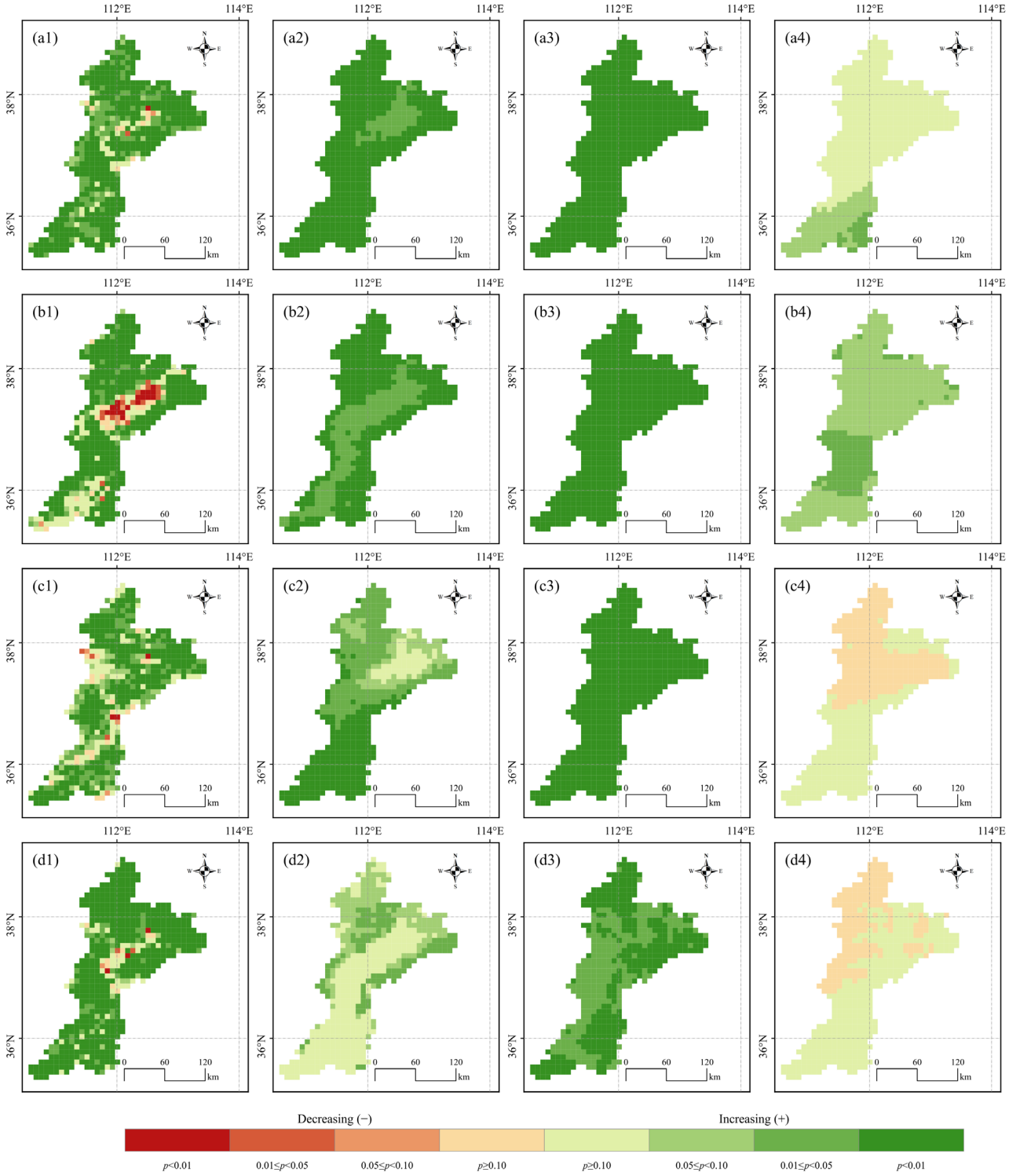


Figure 3. Geographic patterns of temporal trends in kNDVI and climatic variables across the Fen River Basin. (**a1–a4**) kNDVI, PRE, TEM and SR in the growing season; (**b1–b4**) kNDVI, PRE, TEM and SR in spring; (**c1–c4**) kNDVI, PRE, TEM and SR in summer; (**d1–d4**) kNDVI, PRE, TEM and SR in autumn. The significance labels in the figure legend are abbreviated representations of mutually exclusive *p*-value intervals. Pixels were assigned to the most stringent significance category satisfied by their *p*-values. Accordingly, the categories labeled $p < 0.01$, $p < 0.05$, $p < 0.10$, and $p > 0.10$ correspond to $p < 0.01$, $0.01 \leq p < 0.05$, $0.05 \leq p < 0.10$, and $p \geq 0.10$, respectively. The positive (+) and negative (−) categories indicate increasing and decreasing trends based on the sign of the Theil–Sen slope. Each pixel belongs to only one category.

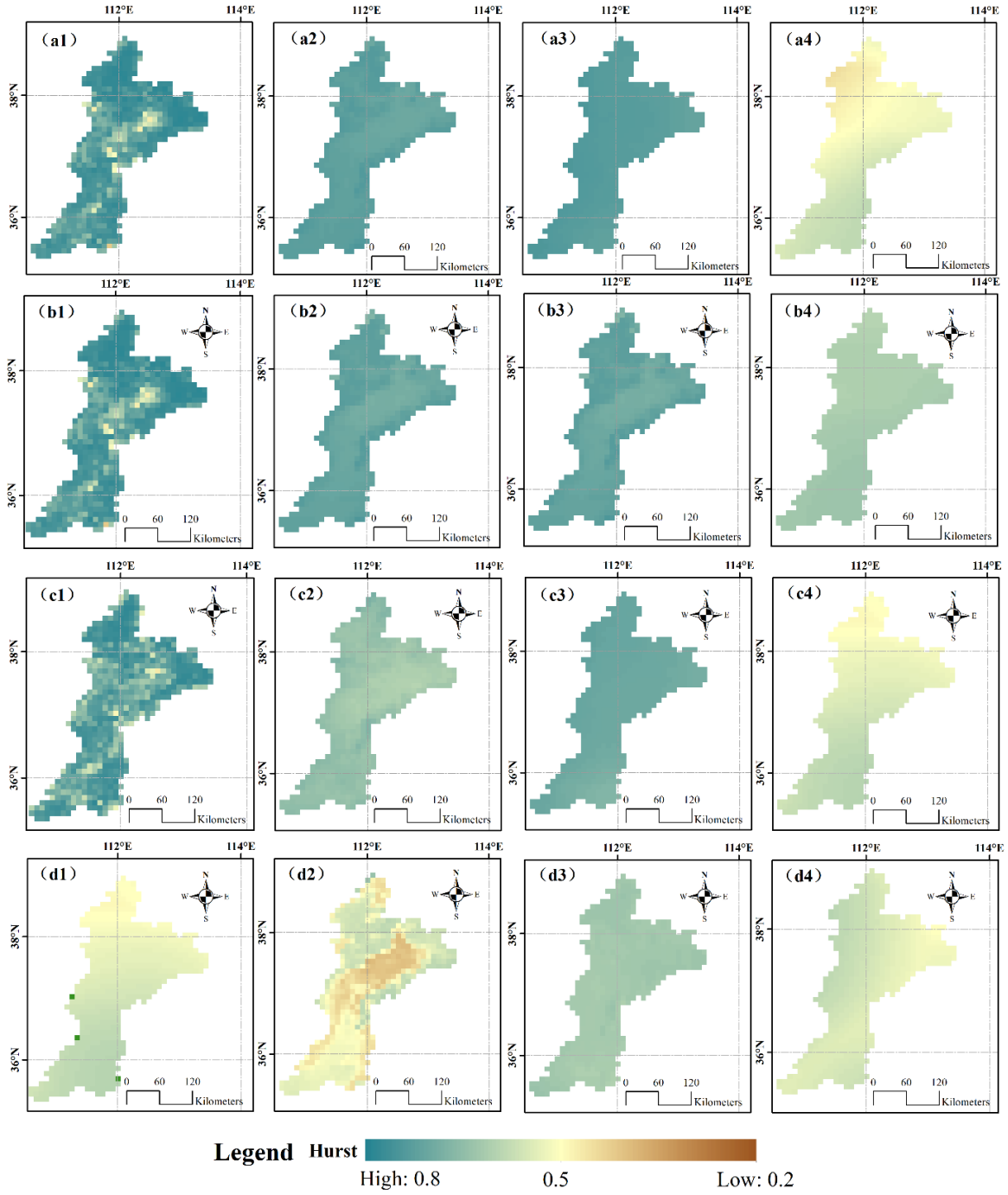


Figure 4. Spatial distribution of Hurst index of kNDVI and climatic factors trends for the 1982–2022 period in the Fen River Basin. (**a1**–**a4**) kNDVI, PRE, TEM and SR in the growing season; (**b1**–**b4**) kNDVI, PRE, TEM and SR in spring; (**c1**–**c4**) kNDVI, PRE, TEM and SR in summer; (**d1**–**d4**) kNDVI, PRE, TEM and SR in autumn.

3.3. Vegetation–Climate Interactions During the Growing Season

3.3.1. Response Mechanisms of Vegetation Dynamics to Climatic Drivers

We implemented partial correlation coefficients (PCCs) to isolate the vegetation–climate relationships by controlling for covarying effects among meteorological variables (Figure 5). For the pixel-wise analysis, significance was corrected for multiple comparisons using the Benjamini–Hochberg FDR ($p < 0.05$). During the growing season, precipitation exhibited a predominantly positive correlation with kNDVI across 92.86% of the basin, with 32.5% of the area demonstrating a statistically significant ($p < 0.05$) strong positive association.

These regions were primarily located in agricultural zones distant from urban centers but subject to frequent residual-based anthropogenic influences. Conversely, only 7.14% of the basin displayed a negative correlation, with merely 0.92% showing a significant negative correlation. Regarding temperature, approximately 98.78% of the basin exhibited a positive correlation with kNDVI, of which 78.9% reached statistical significance, particularly in the middle and upper reaches. A notable exception was observed in the vicinity of Taiyuan, the provincial capital, where urbanization levels are more advanced; here, approximately 0.55% of the area showed a significant negative correlation. In contrast, solar radiation demonstrated a weak overall association with kNDVI, with only 4.75% of the FRB displaying a statistically significant correlation.

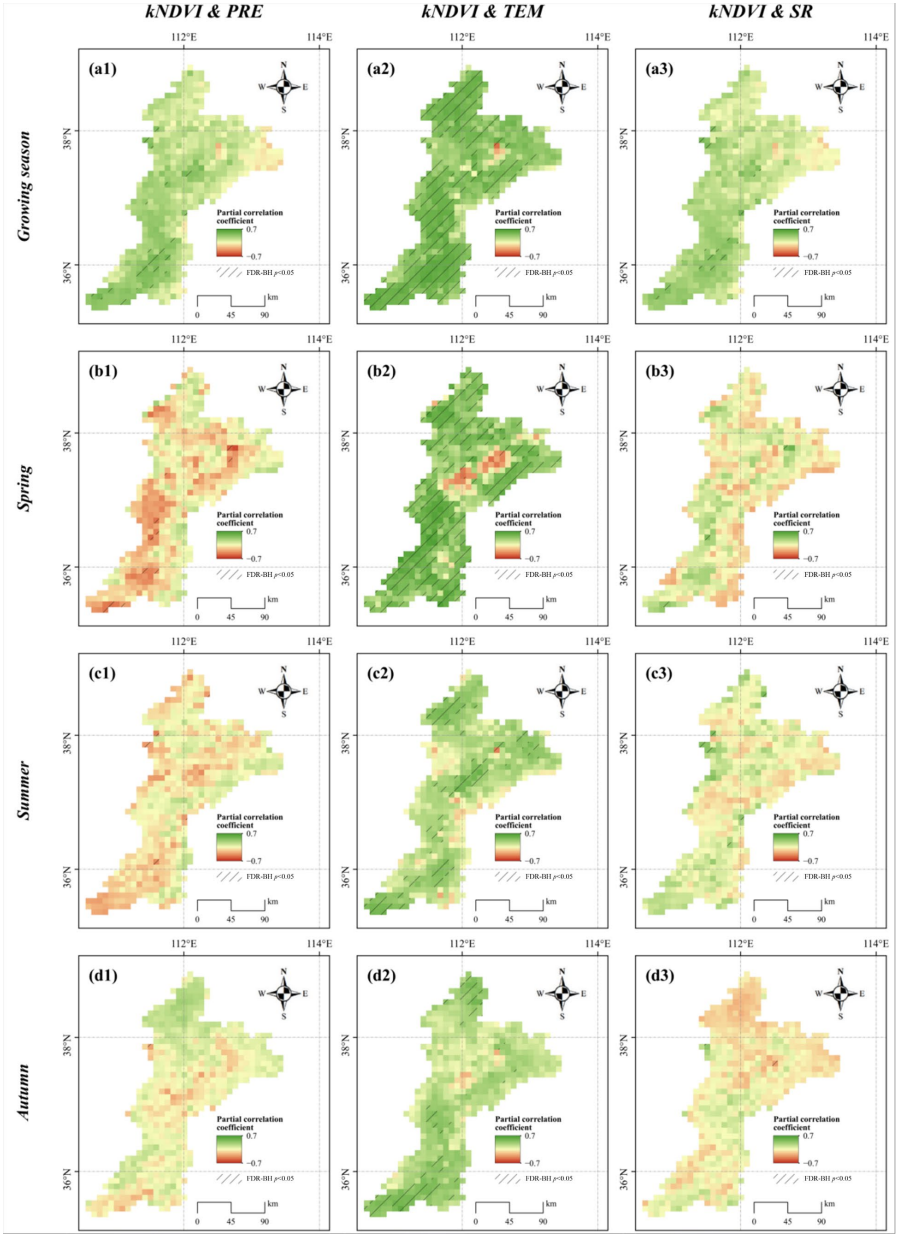


Figure 5. Geospatial patterns of partial correlation between vegetation dynamics (kNDVI) and climatic variables in the Fen River Basin (1982–2022) (**a1**–**a3**) between kNDVI, PRE, TEM, and SR in the growing season; (**b1**–**b3**) kNDVI, PRE, TEM, and SR in spring; (**c1**–**c3**) kNDVI, PRE, TEM, and SR in summer; (**d1**–**d3**) kNDVI, PRE, TEM, and SR in autumn.

An analysis of Figure 5 further indicates limited statistically significant precipitation associations across spring, summer, and autumn, occupying 2.64%, 1.04%, and 0.17% of

the raster-mask area, respectively. Conversely, the mean temperatures during summer and autumn exhibit robust positive correlations with KNDVI, significantly promoting vegetation growth across 90.71% and 96.34% of the basin, respectively. Significant positive temperature associations occupied 18.22% in summer and 15.83% in autumn, compared with 60.26% in spring. Solar-radiation associations varied in direction among seasons, and their total significant areas were limited to 0.88% in spring, 1.56% in summer, and 0.35% in autumn. These results describe seasonal differences in conditional statistical associations; they do not demonstrate radiation-induced physiological constraints or temperature-driven stimulation of vegetation growth.

3.3.2. Climate-Driven Vegetation Dynamics

Figure 6 illustrates the geographic patterns of multiple correlation coefficients (MCCs) linking kNDVI with principal climatic parameters (precipitation, temperature, and solar radiation) throughout the FRB. Colors represent the magnitude of the joint linear association, whereas hatching identifies statistical significance under the conventional F-test. During the growing season, vegetation cover across most of the basin demonstrates significant sensitivity to climate variability, with approximately 77.86% of the area exhibiting statistically significant MCCs ($p < 0.05$); these regions are predominantly concentrated in the northern and eastern sectors. At the seasonal scale, the spatial extent of significant climatic influence diminishes. In contrast, significant MCCs are observed over approximately 80.55%, 39.43%, and 25.55% of the basin area in spring, summer, and autumn, respectively. The significant area was therefore greatest in spring, followed by the growing season, summer, and autumn.

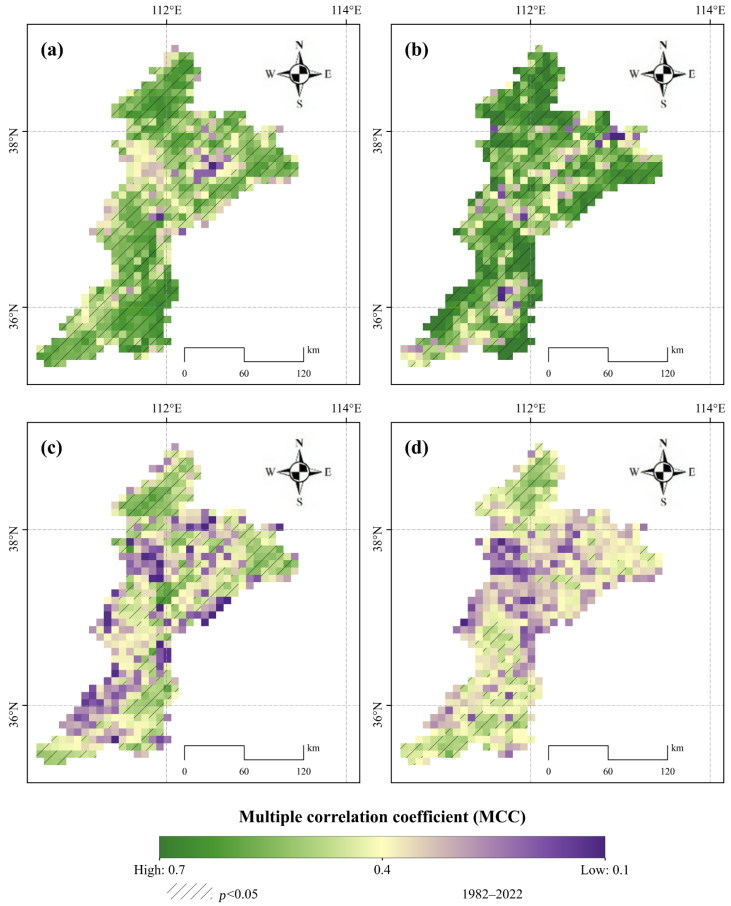


Figure 6. The geospatial distribution of multivariate vegetation–climate relationships was quantified through multiple correlation coefficients (MCCs) across the Fen River Basin (1982–2022): (**a**) growing season; (**b**) spring; (**c**) summer; (**d**) autumn.

Spatially, higher MCCs occur in the northern and eastern regions during spring and summer, shifting to primarily northern and southern zones in autumn. Within these high-correlation areas, kNDVI generally exhibits a positive response to increased precipitation and mean temperature but decreases with higher sunshine duration. Notably, this relationship diverges in highly urbanized areas, such as the Taiyuan Basin, where increased meteorological factors do not correspond to elevated kNDVI values.

3.4. Effects of Climatic Factors and Anthropogenic Influences on kNDVI Variations

Through residual trend analysis and contribution assessment (Table 1), we systematically differentiated the individual impacts of climatic variations and anthropogenic factors on vegetation changes (kNDVI) across the FRB. Spatial patterns of the dominant drivers at the pixel scale are presented in Figure 7, revealing considerable spatial heterogeneity in vegetation responses attributable to these factors. During the growing season, both CC and RBAI synergistically promoted vegetation growth across 95.6% of the basin. Conversely, vegetation degradation within the Taiyuan and Jinzhong urban cores was significantly driven by the combined negative impacts of both CC and RBAI. A seasonal analysis further demonstrated that the proportion of the basin experiencing concurrent positive CC and RBAI influences was highest in autumn (94.4%), followed by spring (85.1%) and summer (84.1%). Notably, spring exhibited an 8.6% area where both CC and RBAI exerted negative effects, primarily concentrated within the intensively developed Taiyuan Basin and potentially linked to agricultural practices and construction. In summer, RBAI positively influenced kNDVI across approximately 11% of the area, predominantly in the western and eastern mountainous regions, likely reflecting benefits from afforestation initiatives.

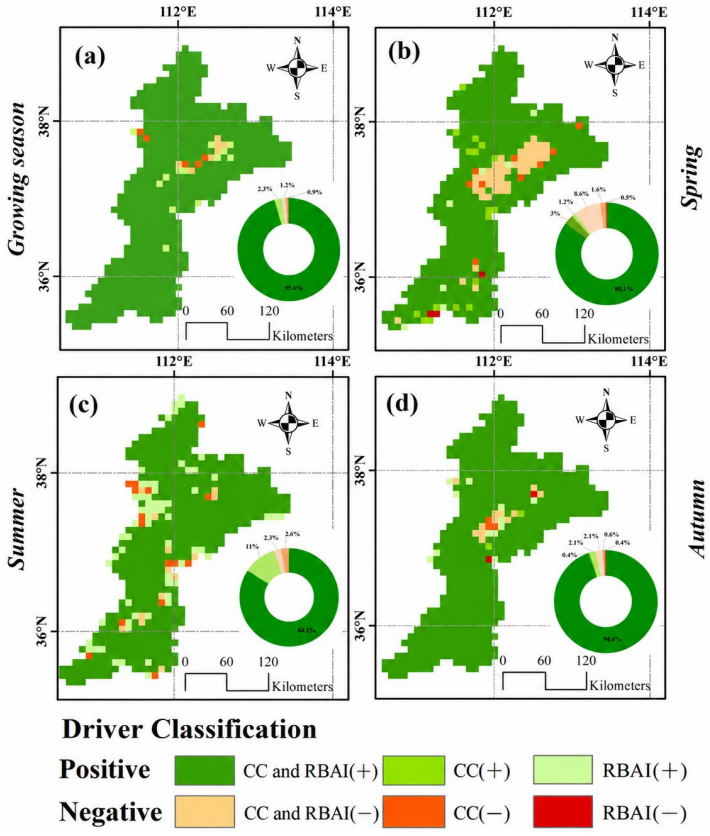


Figure 7. Geographic patterns of vegetation variation causes (CC = climate change, RBAI = residual-based anthropogenic influences) in Fen River Basin (1982–2022) during (**a**) the growing season, (**b**) spring, (**c**) summer, and (**d**) autumn.

Quantitative assessment using the residual and contribution analysis framework revealed that climate variables explained 41.6% of vegetation greening, while the residual component accounted for 58.4%, indicating a dominant contribution from non-climatic factors that are mainly associated with anthropogenic influences under the RESTREND framework (Figure 8). Spatially, CC exerted a positive influence on vegetation dynamics in 98.0% of the basin area. Within these positively affected zones, CC contributions fell predominantly within the 40%–60% range (61.5% of total FRB area), while 5.8% of the area exhibited contributions exceeding 60%. Adverse CC impacts were confined to 1.2% of the basin, primarily concentrated in Jinzhong. Conversely, RBAI positively influenced kNDVI changes in 97.7% of the FRB, with 51.7% of the total area experiencing RBAI contributions between 40% and 60%. Negative RBAI impacts affected 1.4% of vegetated areas, displaying a spatial distribution markedly similar to that of CC-induced degradation.

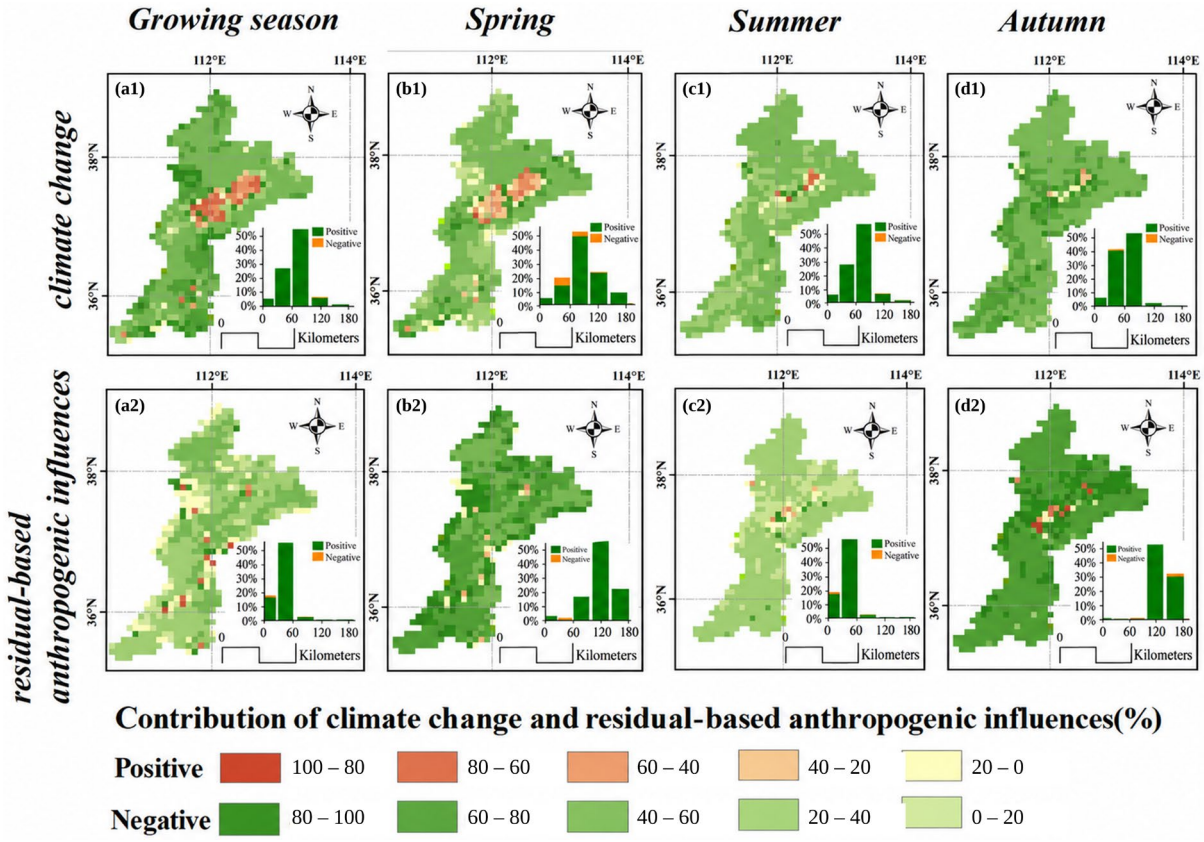


Figure 8. Geographic distribution of vegetation change drivers in the Fen River Basin (1982–2022). (**a1**–**d1**) Climate effects and (**a2**–**d2**) human impacts across seasons.

Seasonal analysis demonstrated distinct temporal patterns: CC constituted the primary driver of spring vegetation changes (55.9% contribution), whereas RBAI dominated in summer (60.3%) and autumn (61.7%). The proportion of kNDVI increase attributed to RBAI was 31.6% (spring), 60.3% (summer), and 61.7% (autumn). Seasonally, CC positively influenced vegetation in 90.8% (spring), 98.8% (summer), and 97.4% (autumn) of the area of the basin, paralleled by RBAI positive impacts in 90.9%, 97.2%, and 97.4% of the area, respectively. Contribution magnitude distributions further diverged seasonally: spring CC contributions peaked in the 40%–60% range (42.9% of area), while summer (46.4%) and autumn (79.0%) peaked in the 20%–40% range. RBAI contributions concentrated in the 40%–60% range during spring (48.0% of area), shifting to the 60%–80% range in summer (56.9%) and autumn (63.4%).

4. Discussion

4.1. Climate Forcing and Vegetation Feedback Mechanisms

This study comprehensively investigates the spatiotemporal evolution of vegetation dynamics (kNDVI) and climatic drivers across multiple time scales in the FRB since the 1980s. We quantify long-term trends and assess shifts following ecological project implementation, analyze kNDVI sensitivity to key climate variables (precipitation, temperature, solar radiation), and rigorously partition the relative effects of CC and RBAI on vegetation shifts—providing critical insights for evaluating GGP efficacy. Methodologically, this work advances prior research by incorporating a broader suite of climate variables (beyond conventional temperature/precipitation focus) and utilizing updated, extended-duration kNDVI data (1982–2022; surpassing earlier NDVI-based studies typically ending in 2015).

The results demonstrate widespread vegetation greening across the Fen River Basin during the 1982–2022 period, as indicated by a significant basin-mean growing-season kNDVI trend of 0.0029 yr^{-1} ($p < 0.01$). At the pixel level, 90.74% of the basin area exhibited statistically significant increasing trends in kNDVI ($p < 0.01$)—consistent with documented vegetation recovery in the broader Loess Plateau and Yellow River Basin [32,59]. Critically, implementation of the GGP post-2000 accelerated these gains: growing season kNDVI trends increased from near-zero pre-2000 to 0.0052 yr^{-1} (2000–2022), accompanied by significant positive trends in spring (0.0028 yr^{-1}), summer (0.0062 yr^{-1}), and autumn (0.0037 yr^{-1}) [26,60]. Such vegetation enhancement overlapped temporally with the implementation of the GGP, implying that ecological restoration projects may be an important driving factor for vegetation greening. Notably, rapid urbanization has concurrently driven localized vegetation degradation, particularly within urban cores, underscoring the imperative to reconcile urban expansion with ecological conservation strategies [25].

The FRB has undergone significant warming and wetting trends during both the growing season and individual seasons over the past four decades [26,47]. These climatic changes, combined with spatial variations in water, heat, and light conditions, have contributed to substantial heterogeneity in the basin's vegetation landscape [61]. Water availability emerges as the primary limiting factor for vegetation growth across most of the FRB's middle and upper reaches, which experience arid to semi-arid conditions [48,62]. This is evidenced by the significant positive correlation ($p < 0.05$) between kNDVI and precipitation in 32.5% of the basin's vegetated areas during the growing season, highlighting vegetation's high sensitivity to water availability. However, seasonal-scale correlations between vegetation and precipitation remain relatively weak, likely due to both the basin's pronounced hydrological seasonality and widespread irrigation practices [5]. The FRB's heavy reliance on irrigation has substantially reduced crop dependence on natural precipitation. This attenuated relationship is likely attributable to the pronounced seasonality of basin hydrology: approximately 80% of annual precipitation occurs during the June–September flood season, creating significant water deficits during the critical April–May crop sowing and seedling establishment phase. Furthermore, although the flood season coincides with peak crop growth, precipitation is predominantly characterized by short-duration, high-intensity events, resulting in limited effective water availability. In well-watered regions, temperature serves as the dominant control on plant growth, where warming can positively influence vegetation by extending the growing season and accelerating development. Conversely, in water-limited areas, temperature increases may exacerbate water stress through enhanced evapotranspiration, ultimately suppressing vegetation growth [63]. Solar radiation exhibits similarly complex effects: while promoting greening in mountainous zones, it can intensify water stress in arid and semi-arid regions through increased evapotranspiration [62]. Vegetation restoration, while beneficial for temperature regulation and hydrological cycling, may intensify water shortages in the FRB

through enhanced evapotranspiration. This concern is substantiated by research showing that the Yellow River Basin's revegetation is approaching regional water carrying capacity thresholds [12,13]. These findings underscore the need for integrated water resource management in the FRB, balancing ecological protection with sustainable water use. Future strategies should carefully consider the basin's water budget—including generation, utilization, and consumption—to ensure vegetation growth remains within sustainable water availability limits [36].

4.2. Effects of Climatic Variations and Anthropogenic Factors on Vegetation Dynamics

Vegetation dynamics in watershed ecosystems are primarily governed by climatic variations and anthropogenic influences. Our residual trend analysis demonstrated that both climate change (CC) and residual-based anthropogenic influences (RBAI) substantially affected plant growth patterns in the FRB, with RBAI (58.4%) showing greater impact magnitude than CC (41.6%). This contrasts with findings from the Loess Plateau, where CC accounted for a larger proportion (55.8%) of vegetation changes compared to RBAI (44.2%) [64]. The discrepancy likely stems from the intensive implementation of regional ecological restoration projects, such as the Grain for Green Program (GGP), which have amplified the impact of human interventions in the FRB.

Seasonal attribution analysis further highlighted distinct temporal patterns in driving forces. In spring, CC was the primary factor (55.9% contribution), likely due to its control over temperature and precipitation during the early growing season. In contrast, RBAI dominated in summer (60.3%) and autumn (61.7%), reflecting the cumulative effects of agricultural practices, afforestation, and land-use management. These findings underscore the need for seasonally differentiated ecological policies to optimize vegetation restoration efforts.

Spatially, RBAI exhibited pronounced effects in urban centers and mountainous regions, with divergent impacts on vegetation growth (Figure 9). Land-use changes from 1980 to 2020 were marked by a decline in cropland and water areas and an expansion of construction land and forests, driven largely by ecological policies [65]. During the 2000–2020 period, a net conversion of approximately 208 km^2 from farmland to forest and grassland was observed, providing evidence consistent with a possible contribution from policy-driven ecological restoration, including the Grain for Green Program (GGP) [66]. Urbanization also emerged as a critical factor, with rapid urban expansion leading to vegetation degradation in and around cities. The conversion of farmland to construction land highlights the trade-offs between development and ecological preservation [67]. These findings emphasize the dual role of residual-based anthropogenic influences—both restorative and destructive—and the need for balanced land-use planning to harmonize socioeconomic growth with ecosystem sustainability.

Our previously published study only briefly presented seasonal statistics without systematically interpreting the divergent driving mechanisms across spring, summer, and autumn [48]. In this work, we revealed a critical seasonal shift of dominant drivers: spring vegetation variations are mainly climate-driven, whereas summer and autumn vegetation changes are dominated by human-related restoration activities. Furthermore, we explained the underlying physical reasons for such seasonal divergence: spring vegetation growth is highly constrained by pre-growing-season hydrothermal conditions; by contrast, the cumulative effects of afforestation, land use conversion and agricultural management gradually dominate vegetation performance in summer and autumn. This mechanistic interpretation is absent from our previous study. Compared with the previous paper, we added a quantitative land-use transfer analysis across the 1980–2020 period. By linking land use conversion magnitudes (farmland-to-forest/grassland after GGP) with pixel-scale

attribution results, we connect the statistical attribution outputs with real land-policy practice. This strengthens the physical interpretation of human-driven vegetation changes, which was not systematically realized in our earlier work.

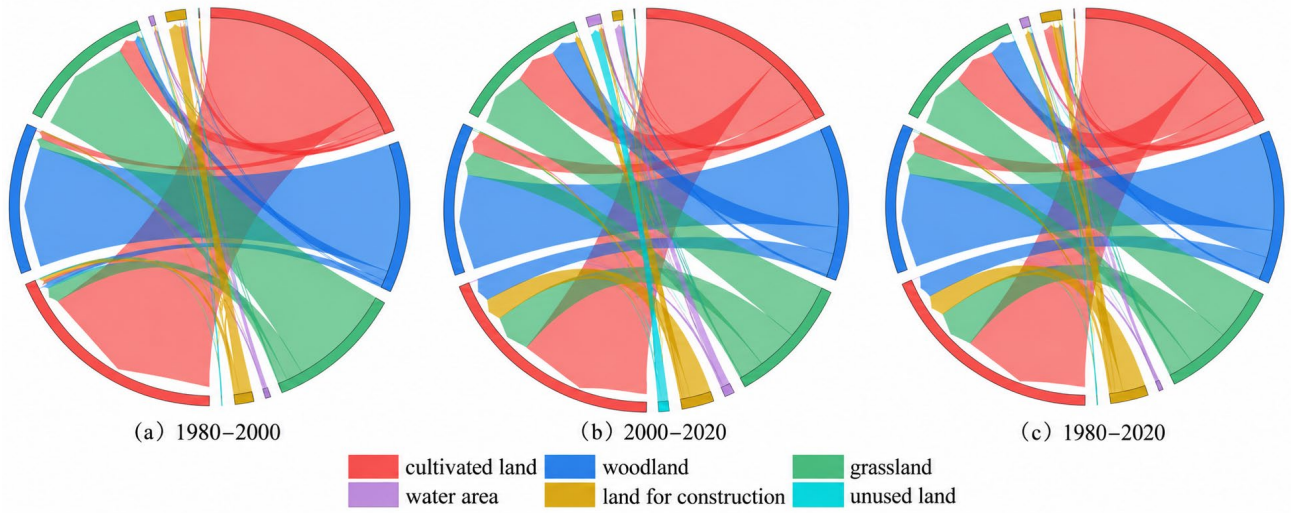


Figure 9. Spatial patterns of land use change in the Fen River Basin (**a**) from 1980 to 2000; (**b**) from 2000 to 2020; (**c**) from 1980 to 2020.

4.3. Potential and Uncertainty

Although this study provides insights into long-term vegetation dynamics and their seasonal drivers in the Fen River Basin (FRB), several uncertainties should be acknowledged. First, residual trend analysis (RESTREND) statistically separates vegetation variation into a climate-predicted component and an unexplained residual component. Although residual trends may contain signals associated with ecological restoration, land-use change, irrigation, and other human activities, they may also reflect omitted environmental factors, natural disturbances, satellite-observation uncertainty, and model errors. Therefore, the residual-based anthropogenic influence (RBAI) should be interpreted as an indicator of potential human influence rather than a direct measure of anthropogenic effects. Accordingly, the estimated contributions of the climate-predicted and residual components represent model-dependent statistical estimates rather than precise causal contributions. The observed vegetation greening and land-use transitions after 2000 are consistent with a possible contribution from ecological restoration, including the Grain for Green Program (GGP), but the independent causal effect of this policy cannot be isolated using the present approach.

Second, although the multiple-linear-regression-based RESTREND framework provides a transparent and interpretable approach for long-term vegetation attribution and facilitates comparisons across seasons, its linear specification may not fully capture complex vegetation–climate relationships. Vegetation responses to precipitation, temperature, and solar radiation may involve nonlinear thresholds, saturation effects, interactions, and time-lagged responses, particularly under water limitation or thermal stress. These unmodeled climatic responses may enter the residual component and influence the estimated relative contributions. Future research will consider generalized additive models (GAMs) and interpretable machine-learning approaches to characterize these nonlinear relationships and evaluate the sensitivity of attribution results to alternative model structures.

Finally, the relatively coarse spatial resolution of GIMMS-3G+ (0.0833°) limits the representation of localized urbanization, heterogeneous agricultural landscapes, and fine-scale topographic variability, although its long-term consistency is valuable for basin-scale analysis. In addition, temporal autocorrelation and multiple pixel-wise statistical tests

may affect the interpretation of nominal significance levels. Further integration of higher-resolution remote sensing observations, additional environmental variables, and more rigorous statistical validation would help improve the robustness and spatial specificity of vegetation-change assessments.

5. Conclusions

We comprehensively investigated vegetation patterns across the FRB from 1982 to 2022, examining both spatial and temporal variations. The study evaluated how vegetation responds to shifting climatic conditions while employing quantitative methods to separate and compare the climate versus anthropogenic influences on vegetation dynamics.

Over the past four decades, vegetation exhibited significant increasing trends across the FRB. The growing-season kNDVI increased at an annual rate of 0.0029 yr^{-1}, with 90.74% of the area exhibiting a marked progressive rise ($p < 0.01$). A total of 99.12% of the basin exhibited persistent temporal behavior in growing-season kNDVI (Hurst index > 0.5). Seasonal analysis revealed consistent growth in spring, summer, and autumn, with the most pronounced improvement occurring after the implementation of the Grain for Green Program (GGP), which helped accelerate to a 23.1% increase in kNDVI. Concurrently, precipitation and temperature showed significant upward trends ($p < 0.05$ and $p < 0.01$, respectively), while solar radiation exhibited a weaker, non-significant increase ($p > 0.1$). Partial correlation analysis indicated that 92.86% of the basin exhibited a positive correlation between kNDVI and precipitation, with 32.5% showing strong significance, particularly in agricultural zones. Similarly, 98.78% of the basin displayed a positive correlation with temperature, of which 78.9% was significant, primarily in the middle and upper reaches. In contrast, solar radiation showed minimal correlation (only 4.75% significant). The relative contributions of the climate and anthropogenic influences were quantified at 41.6% and 58.4% to kNDVI changes. Within the RESTREND framework, both the climate-predicted and residual components contributed positively to vegetation greening across 95.6% of the basin. Seasonal variations revealed distinct dominant drivers: CC was the primary influence in spring (55.9%), whereas RBAI dominated in the summer (60.3%) and autumn (61.7%). These findings highlight the seasonally dependent interplay between climatic and anthropogenic factors in shaping vegetation dynamics. Notably, the GGP and other ecological restoration efforts have played a pivotal role in enhancing vegetation cover, particularly in the summer and autumn, underscoring the effectiveness of policy-driven interventions. These results significantly advance the understanding of vegetation–climate–human interactions in ecologically vulnerable basins and provide critical insights for optimizing ecological conservation strategies. Such efforts will be essential for guiding adaptive management in the FRB and similar regions under global environmental change.

Author Contributions: Conceptualization, K.N. and H.W.; Methodology, C.Z. and K.N.; Software, K.N.; Validation, C.Z.; Formal analysis W.Z.; Data curation, K.N.; Writing—original draft preparation, K.N.; Writing—review and editing, H.W. and C.Z.; Visualization, K.N.; supervision, H.W. and C.Z.; Funding acquisition, C.Z. and K.N. All authors have read and agreed to the published version of the manuscript.

Funding: The project was supported by Yunnan Fundamental Research Projects (grant no. 202601CF070043), the National Natural Science Foundation of China (no. 52669002), and the Basic Research Project of Shanxi Province (202303021212381), and the Shanxi Provincial Key Laboratory of Surface Processes and Resource Ecological Security in the Fen River Basin Open Fund Project (FHKF2022409).

Data Availability Statement: The Global Vegetation Greenness Index and the Normalized Difference Vegetation Index (NDVI) from AVHRR GIMMS-3G+ (1982–2022) are available at https:

//daac.ornl.gov/cgi-bin/dsviewer.pl?ds_id=2187, accessed on 20 October 2023. The 1 km monthly precipitation dataset for China (1901–2022) is available at https://data.tpdc.ac.cn/zh-hans/data/faae7605-a0f2-4d18-b28f-5cee413766a2, accessed on 20 October 2023. The 1 km monthly mean temperature dataset for China (1901–2022) is available at https://data.tpdc.ac.cn/zh-hans/data/71ab4677-b66c-4fd1-a004-b2a541c4d5bf, accessed on 20 October 2023. The Terra Climate data are available at https://developers.google.cn/earth-engine/datasets/catalog/IDAHO_EPSCOR_TERRACLIMATE?hl=zh-cn, accessed on 20 October 2023. The land use data are available at https://www.resdc.cn, accessed on 20 October 2023.

Conflicts of Interest: Author Houfa Wu was employed by the company Changjiang Institute of Survey, Planning, Design and Research, Wuhan, China. The remaining authors declare that the research was conducted in the absence of any commercial or financial relationships that could be construed as a potential conflict of interest.

References

1. Mottl, O.; Flantua, S.G.; Bhatta, K.P.; Felde, V.A.; Giesecke, T.; Goring, S.; Grimm, E.C.; Haberle, S.; Hooghiemstra, H.; Ivory, S. Global acceleration in rates of vegetation change over the past 18,000 years. *Science* **2021**, *372*, 860–864, Correction in *Science* **2021**, *373*, eabk222. https://doi.org/10.1126/science.abk2221. [CrossRef] [PubMed]
2. Zeng, Y.; Hao, D.; Huete, A.; Dechant, B.; Berry, J.; Chen, J.M.; Joiner, J.; Frankenberg, C.; Bond-Lamberty, B.; Ryu, Y. Optical vegetation indices for monitoring terrestrial ecosystems globally. *Nat. Rev. Earth Environ.* **2022**, *3*, 477–493. [CrossRef]
3. Cheng, M.; Wang, Z.; Wang, S.; Liu, X.; Jiao, W.; Zhang, Y. Determining the impacts of climate change and human activities on vegetation change on the Chinese Loess Plateau considering human-induced vegetation type change and time-lag effects of climate on vegetation growth. *Int. J. Digit. Earth* **2024**, *17*, 2336075. [CrossRef]
4. Forzieri, G.; Dakos, V.; McDowell, N.G.; Ramdane, A.; Cescatti, A. Emerging signals of declining forest resilience under climate change. *Nature* **2022**, *608*, 534–539. [CrossRef] [PubMed]
5. Zhan, C.; Liang, C.; Zhao, L.; Jiang, S.; Niu, K.; Zhang, Y.; Cheng, L. Detection and attribution of vegetation dynamics in the National Barrier Zone of China by considering climate temporal effects. *Int. J. Appl. Earth Obs. Geoinf.* **2023**, *116*, 103140. [CrossRef]
6. Bellini, E.; Moriondo, M.; Dibari, C.; Leolini, L.; Staglianò, N.; Stendardi, L.; Filippa, G.; Galvagno, M.; Argenti, G. Impacts of climate change on European grassland phenology: A 20-year analysis of MODIS satellite data. *Remote Sens.* **2022**, *15*, 218. [CrossRef]
7. Wang, Y.; Peng, L.; Yue, Y.; Chen, T. Global vegetation-temperature sensitivity and its driving forces in the 21st century. *Earth's Future* **2024**, *12*, e2022EF003395. [CrossRef]
8. Jokar, P.; Masoudi, M. Evaluation of ecological capability and land use planning for different uses of land with a new model of EMOLUP in Jahrom County, Iran. *Front. Earth Sci.* **2023**, *17*, 561–575. [CrossRef]
9. Razaghi, S.; Masoudi, M. Developing a new model for ecological capability evaluation of irrigated agriculture using GIS in Sepidan Township, Iran. *Process Integr. Optim. Sustain.* **2024**, *8*, 845–855. [CrossRef]
10. Chen, Y.; Zhang, T.; Zhu, X.; Yi, G.; Li, J.; Bie, X.; Hu, J.; Liu, X. Quantitatively analyzing the driving factors of vegetation change in China: Climate change and human activities. *Ecol. Inform.* **2024**, *82*, 102667. [CrossRef]
11. Wang, K.; Fu, C.; Zhao, C.; Zhou, T.; Lian, Y.; Wang, G. Vegetation change mechanism and key driving factors in complex terrains, China. *Sci. Total Environ.* **2025**, *979*, 179424. [CrossRef] [PubMed]
12. Ma, Y.; Wang, W.; Jin, S.; Li, H.; Liu, B.; Gong, W.; Fan, R.; Li, H. Spatiotemporal variation of LAI in different vegetation types and its response to climate change in China from 2001 to 2020. *Ecol. Indic.* **2023**, *156*, 111101. [CrossRef]
13. Zhou, J.; Liu, Q.; Liang, L.; Yan, D.; Yang, Y.; Wang, X.; Sun, T.; Li, S.; Gan, L.; Wu, J. Water constraints enhanced by revegetation while alleviated by increased precipitation on China's water-dominated Loess Plateau. *J. Hydrol.* **2024**, *640*, 131731. [CrossRef]
14. Stagakis, S.; Markos, N.; Sykioti, O.; Kyparissis, A. Monitoring canopy biophysical and biochemical parameters in ecosystem scale using satellite hyperspectral imagery: An application on a Phlomis fruticosa Mediterranean ecosystem using multiangular CHRIS/PROBA observations. *Remote Sens. Environ.* **2010**, *114*, 977–994. [CrossRef]
15. Matsushita, B.; Yang, W.; Chen, J.; Onda, Y.; Qiu, G. Sensitivity of the enhanced vegetation index (EVI) and normalized difference vegetation index (NDVI) to topographic effects: A case study in high-density cypress forest. *Sensors* **2007**, *7*, 2636–2651. [CrossRef] [PubMed]
16. Camps-Valls, G.; Campos-Taberner, M.; Moreno-Martínez, Á.; Walther, S.; Duveiller, G.; Cescatti, A.; Mahecha, M.D.; Muñoz-Marí, J.; García-Haro, F.J.; Guanter, L. A unified vegetation index for quantifying the terrestrial biosphere. *Sci. Adv.* **2021**, *7*, eabc7447. [CrossRef] [PubMed]

17. Wang, C.; Liu, L.; Zhou, Y.; Liu, X.; Wu, J.; Tan, W.; Xu, C.; Xiong, X. Comparison between satellite derived solar-induced chlorophyll fluorescence, NDVI and kNDVI in detecting water stress for dense vegetation across southern China. *Remote Sens.* **2024**, *16*, 1735. [CrossRef]
18. Feng, X.; Tian, J.; Wang, Y.; Wu, J.; Liu, J.; Ya, Q.; Li, Z. Spatio-temporal variation and climatic driving factors of vegetation coverage in the Yellow River Basin from 2001 to 2020 based on kNDVI. *Forests* **2023**, *14*, 620. [CrossRef]
19. Wang, Q.; Moreno-Martínez, Á.; Muñoz-Marí, J.; Campos-Taberner, M.; Camps-Valls, G. Estimation of vegetation traits with kernel NDVI. *ISPRS J. Photogramm. Remote Sens.* **2023**, *195*, 408–417. [CrossRef]
20. Wu, Z.; Yao, F.; Ahmad, A.; Deng, F.; Fang, J. Spatiotemporal Evolution and Driving Mechanisms of kNDVI in Different Sections of the Yangtze River Basin Using Multiple Statistical Methods and the PLSPM Model. *Remote Sens.* **2025**, *17*, 299. [CrossRef]
21. Conradi, T.; Eggli, U.; Kreft, H.; Schweiger, A.H.; Weigelt, P.; Higgins, S.I. Reassessment of the risks of climate change for terrestrial ecosystems. *Nat. Ecol. Evol.* **2024**, *8*, 888–900. [CrossRef] [PubMed]
22. Higgins, S.I.; Conradi, T.; Muhoko, E. Shifts in vegetation activity of terrestrial ecosystems attributable to climate trends. *Nat. Geosci.* **2023**, *16*, 147–153, Correction in *Nat. Geosci.* **2023**, *16*, 546. https://doi.org/10.1038/s41561-023-01196-1. [CrossRef]
23. Nolan, C.; Overpeck, J.T.; Allen, J.R.; Anderson, P.M.; Betancourt, J.L.; Binney, H.A.; Brewer, S.; Bush, M.B.; Chase, B.M.; Cheddadi, R. Past and future global transformation of terrestrial ecosystems under climate change. *Science* **2018**, *361*, 920–923. [CrossRef] [PubMed]
24. Brinkman, R.; Sombroek, W.G. The effects of global change on soil conditions in relation to plant growth and food production. In *Global Climate Change and Agricultural Production*; Bazzaz, F.A., Sombroek, W.G., Eds.; Food and Agriculture Organization of the United Nations: Rome, Italy; John Wiley & Sons: Chichester, UK, 1996; pp. 49–63. Available online: https://www.fao.org/4/W5183E/w5183e05.htm (accessed on 12 January 2023).
25. Liu, J.; Wang, H.; Tang, B.; Hui, L.; Zhang, W.; Zhang, L.; Jiao, L. Analysis of temporal and spatial dynamics of ecosystem services and trade-offs/synergies during urbanization in the Loess Plateau, China. *Land* **2023**, *12*, 2136. [CrossRef]
26. Yang, J.; Huang, X. The 30 m annual land cover datasets and its dynamics in China from 1990 to 2020. *Earth Syst. Sci. Data* **2021**, *13*, 3907–3925. [CrossRef]
27. Liu, X.; Zhu, X.; Pan, Y.; Zhu, W.; Zhang, J.; Zhang, D. Thermal growing season and response of alpine grassland to climate variability across the Three-Rivers Headwater Region, China. *Agric. For. Meteorol.* **2016**, *220*, 30–37. [CrossRef]
28. Masoudi, M.; Asrari, E. Hazard assessment of global warming around the world using GIS. *Environ. Monit. Assess.* **2023**, *195*, 1025. [CrossRef] [PubMed]
29. Masoudi, M.; Asrari, E.; Younesfard, A.R.; Haghighi, A.T. Spatial and statistical analysis of climate change in the middle east: A study of precipitation and temperature variability using NOAA weather data and Geostatistical methods. *Earth Syst. Environ.* **2025**, *9*, 3551–3579. [CrossRef]
30. Peng, X.; Zhang, T.; Frauenfeld, O.W.; Wang, S.; Qiao, L.; Du, R.; Mu, C. Northern Hemisphere greening in association with warming permafrost. *J. Geophys. Res. Biogeosci.* **2020**, *125*, e2019JG005086. [CrossRef]
31. Piao, S.; Friedlingstein, P.; Ciais, P.; Zhou, L.; Chen, A. Effect of climate and CO_2 changes on the greening of the Northern Hemisphere over the past two decades. *Geophys. Res. Lett.* **2006**, *33*, L23402. [CrossRef]
32. Fan, X.; Qu, Y.; Zhang, J.; Bai, E. China's vegetation restoration programs accelerated vegetation greening on the Loess Plateau. *Agric. For. Meteorol.* **2024**, *350*, 109994. [CrossRef]
33. Bodner, G.; Nakhforoosh, A.; Kaul, H.-P. Management of crop water under drought: A review. *Agron. Sustain. Dev.* **2015**, *35*, 401–442. [CrossRef]
34. Lian, X.; Piao, S.; Chen, A.; Huntingford, C.; Fu, B.; Li, L.Z.; Huang, J.; Sheffield, J.; Berg, A.M.; Keenan, T.F.; et al. Multifaceted characteristics of dryland aridity changes in a warming world. *Nat. Rev. Earth Environ.* **2021**, *2*, 232–250. [CrossRef]
35. Jiang, P.; Ding, W.; Yuan, Y.; Ye, W.; Mu, Y. Interannual variability of vegetation sensitivity to climate in China. *J. Environ. Manag.* **2022**, *301*, 113768. [CrossRef] [PubMed]
36. Chen, M.; Xue, Y.; Xue, Y.; Peng, J.; Guo, J.; Liang, H. Assessing the effects of climate and human activity on vegetation change in Northern China. *Environ. Res.* **2024**, *247*, 118233. [CrossRef] [PubMed]
37. Qi, T.; Ren, Q.; He, C.; Zhang, X. Dual effects on vegetation from urban expansion in the drylands of northern China: A multiscale investigation using the vegetation disturbance index. *Sci. Total Environ.* **2024**, *928*, 172481. [CrossRef] [PubMed]
38. Talukdar, S.; Naikoo, M.W.; Rahman, A. Urban expansion and vegetation dynamics: The role of protected areas in preventing vegetation loss in a growing mega city. *Habitat Int.* **2024**, *150*, 103129. [CrossRef]
39. Hu, B.; Zhang, Z.; Han, H.; Li, Z.; Cheng, X.; Kang, F.; Wu, H. The Grain for Green Program intensifies trade-offs between ecosystem services in midwestern Shanxi, China. *Remote Sens.* **2021**, *13*, 3966. [CrossRef]
40. He, L.; Guo, J.; Jiang, Q.; Zhang, Z.; Yu, S. How did the Chinese Loess Plateau turn green from 2001 to 2020? An explanation using satellite data. *Catena* **2022**, *214*, 106246. [CrossRef]

41. Wang, H.; Sun, F. Variability of annual sediment load and runoff in the Yellow River for the last 100 years (1919–2018). *Sci. Total Environ.* **2021**, *758*, 143715. [CrossRef] [PubMed]
42. Yuan, Z.; Pang, Y.; Wang, C.; Meng, S.; Sun, X.; Gu, D. Ecological programs changed the forest landscape pattern in the Yellow River Basin from 2000 to 2020. *Landsc. Ecol.* **2025**, *40*, 100. [CrossRef]
43. Liu, J.; Wei, L.; Zheng, Z.; Du, J. Vegetation cover change and its response to climate extremes in the Yellow River Basin. *Sci. Total Environ.* **2023**, *905*, 167366. [CrossRef] [PubMed]
44. Zhang, J.; Du, J.; Sheng, Z.; Zhang, Y.; Wu, J.; Liu, B. Spatio-temporal changes of vegetation cover and their influencing factors in the Yellow River Basin from 1982 to 2015. *Ecol. Environ.* **2021**, *30*, 929. [CrossRef]
45. Guo, Y.; Zhang, L.; He, Y.; Cao, S.; Li, H.; Ran, L.; Ding, Y.; Filonchyk, M. LSTM time series NDVI prediction method incorporating climate elements: A case study of Yellow River Basin, China. *J. Hydrol.* **2024**, *629*, 130518. [CrossRef]
46. Zhao, X.; Xia, H.; Pan, L.; Song, H.; Niu, W.; Wang, R.; Li, R.; Bian, X.; Guo, Y.; Qin, Y. Drought monitoring over Yellow River basin from 2003–2019 using reconstructed MODIS land surface temperature in Google Earth Engine. *Remote Sens.* **2021**, *13*, 3748. [CrossRef]
47. Zhang, Q.; Yang, J.; Wang, W.; Ma, P.; Lu, G.; Liu, X.; Yu, H.; Fang, F. Climatic warming and humidification in the arid region of Northwest China: Multi-scale characteristics and impacts on ecological vegetation. *J. Meteorol. Res.* **2021**, *35*, 113–127. [CrossRef]
48. Niu, K.; Liu, G.; Zhan, C.; Kang, A. The Role of Climate Change and Human Intervention in Shaping Vegetation Patterns in the Fen River Basin of China: Implications of the Grain for Green Program. *Forests* **2024**, *15*, 1733. [CrossRef]
49. Liu, X.; Zhu, X.; Li, S.; Liu, Y.; Pan, Y. Changes in growing season vegetation and their associated driving forces in China during 2001–2012. *Remote Sens.* **2015**, *7*, 15517–15535. [CrossRef]
50. Peng, S.; Ding, Y.; Liu, W.; Li, Z. 1 km monthly temperature and precipitation dataset for China from 1901 to 2017. *Earth Syst. Sci. Data* **2019**, *11*, 1931–1946. [CrossRef]
51. Peng, S. 1-km Monthly Precipitation Dataset for China (1901–2022); National Tibetan Plateau/Third Pole Environment Data Center. Available online: https://data.tpdc.ac.cn/zh-hans/data/faae7605-a0f2-4d18-b28f-5cee413766a2 (accessed on 20 October 2023).
52. Peng, S. 1-km Monthly Mean Temperature Dataset for China (1901–2022); National Tibetan Plateau/Third Pole Environment Data Center. Available online: https://data.tpdc.ac.cn/zh-hans/data/71ab4677-b66c-4fd1-a004-b2a541c4d5bf (accessed on 20 October 2023).
53. Abatzoglou, J.T.; Dobrowski, S.Z.; Parks, S.A.; Hegewisch, K.C. TerraClimate, a high-resolution global dataset of monthly climate and climatic water balance from 1958–2015. *Sci. Data* **2018**, *5*, 170191. [CrossRef] [PubMed]
54. Abatzoglou, J.T.; Dobrowski, S.Z. TerraClimate; Google Earth Engine Data Catalog. Available online: https://developers.google.cn/earth-engine/datasets/catalog/IDAHO_EPSCOR_TERRACLIMATE?hl=zh-cn (accessed on 20 October 2023).
55. Sen, P.K. Estimates of the regression coefficient based on Kendall's tau. *J. Am. Stat. Assoc.* **1968**, *63*, 1379–1389. [CrossRef]
56. Yue, S.; Wang, C.Y. The Mann–Kendall Test Modified by Effective Sample Size to Detect Trend in Serially Correlated Hydrological Series. *Water Resour. Manag.* **2004**, *18*, 201–218. [CrossRef]
57. Wang, N.; Xu, Z.; Xu, Y.; Yang, Y.; Cong, N.; Yao, W. From climate-driven to dam-regulated: Impacts of dams on riparian vegetation in a mountainous river system. *Catena* **2026**, *265*, 109879. [CrossRef]
58. Ren, Y.; Liu, J.; Liu, S.; Wang, Z.; Liu, T.; Shalamzari, M.J. Effects of climate change on vegetation growth in the Yellow River Basin from 2000 to 2019. *Remote Sens.* **2022**, *14*, 687. [CrossRef]
59. Yin, P.; Li, C.; Wei, Y.; Zhang, L.; Liu, C.; Chen, J.; Liu, Y.; Xiong, X. Impact of relative temperature changes on vegetation growth in China from 2001 to 2017. *J. Clean. Prod.* **2024**, *451*, 142062. [CrossRef]
60. Ni, X.; Guo, W.; Li, X.; Li, S. Heterogeneity of increases in net primary production under intensified human activity and climate variability on the Loess Plateau of China. *Remote Sens.* **2022**, *14*, 4706. [CrossRef]
61. Wang, X.; Shi, S.; Zhao, X.; Hu, Z.; Hou, M.; Xu, L. Detecting spatially non-stationary between vegetation and related factors in the Yellow River Basin from 1986 to 2021 using multiscale geographically weighted regression based on Landsat. *Remote Sens.* **2022**, *14*, 6276. [CrossRef]
62. Xu, Z.; Li, Y.; Qin, Y.; Bach, E. A global assessment of the effects of solar farms on albedo, vegetation, and land surface temperature using remote sensing. *Sol. Energy* **2024**, *268*, 112198. [CrossRef]
63. Qin, G.; Meng, Z.; Fu, Y. Drought and water-use efficiency are dominant environmental factors affecting greenness in the Yellow River Basin, China. *Sci. Total Environ.* **2022**, *834*, 155479. [CrossRef] [PubMed]
64. Li, W.; Zhou, J.; Xu, Z.; Liang, Y.; Shi, J.; Zhao, X. Climate impact greater on vegetation NPP but human enhance benefits after the Grain for Green Program in Loess Plateau. *Ecol. Indic.* **2023**, *157*, 111201. [CrossRef]
65. Yu, H.; Yang, Q.; Jiang, S.; Zhan, B.; Zhan, C. Detection and attribution of vegetation dynamics in the yellow river basin based on long-Term kernel NDVI data. *Remote Sens.* **2024**, *16*, 1280. [CrossRef]

66. Zhang, Q.; Wang, G.; Yuan, R.; Singh, V.P.; Wu, W.; Wang, D. Dynamic responses of ecological vulnerability to land cover shifts over the Yellow River Basin, China. *Ecol. Indic.* **2022**, *144*, 109554. [CrossRef]
67. Li, D.; Wu, S.; Liang, Z.; Li, S. The impacts of urbanization and climate change on urban vegetation dynamics in China. *Urban For. Urban Green.* **2020**, *54*, 126764. [CrossRef]

Disclaimer/Publisher's Note: The statements, opinions and data contained in all publications are solely those of the individual author(s) and contributor(s) and not of MDPI and/or the editor(s). MDPI and/or the editor(s) disclaim responsibility for any injury to people or property resulting from any ideas, methods, instructions or products referred to in the content.